Chemical Science

ROYAL SOCIETY OF CHEMISTRY

EDGE ARTICLE

View Article Online
View Journal

Cite this: DOI: 10.1039/d6sc00776g

All publication charges for this article have been paid for by the Royal Society of Chemistry

Ultrasmooth and thin pheomelanin-like film as a metal-free electrocatalytic enhancer

Chan Yeon Kim, †[a] Jae Ryeol Jeong, †[a] Seong Ah Jo, †[a] Jun Seok Park,[a] Joowon Choi,[a] Myung Jun Kim,[b] Minho Kim, *[a] Kyungtae Kang*[a] and Min Hyung Lee *[a]

Received 28th January 2026
Accepted 26th March 2026

DOI: 10.1039/d6sc00776g

rsc.li/chemical-science

This study explores a bioinspired approach to enhance electrocatalytic oxygen evolution reaction (OER) performance by employing a pheomelanin-like thin film. Inspired by the complex chemistry of natural pigments, we developed an ultrasmooth and exceptionally thin organic coating by introducing cysteine derivatives into dopamine-based solutions. The resulting films, approximately 2 nm thick, form conformal layers on conventional RuO_2 electrocatalysts and significantly reduce the overpotential required for the OER. Specifically, coatings with cysteine methyl ester (CME) or cysteine ethyl ester (CEE) achieved overpotential reductions of up to 34 mV at 10 mA cm^{-2} compared to pristine RuO_2. Beyond improved catalytic performance, the films exhibited unique deposition kinetics characterized by an autocatalytic "bursting" behavior, highlighting the emergent properties of the system. Our findings underscore the potential of bioinspired organic materials to modulate electrocatalytic interfaces, offering new strategies for the rational design of hybrid catalytic systems in energy conversion technologies.

Introduction

Melanin-like polymers are redox-active organic materials that embed persistent carbon-centered and semiquinone-based radicals within a heterogeneous π-conjugated network.[1–4] Subtle variations in the precursor structure and supramolecular association often tune inter-oligomer conjugation and π–π stacking, thereby modulating charge transport and radical chemistry (Fig. 1).[5] In eumelanin, for instance, preventing the spontaneous decarboxylation of 5,6-dihydroxyindole carboxylic acid (*i.e.*, retaining the –COOH instead of forming 5,6-dihydroxyindole, DHI) was shown to impede inter-unit conjugation and reshape the radical character—hence the electron-transfer capability—of the pigment.[6,7] This aligns with the characteristics of a complex system, where simple changes in the initial conditions can lead to emergent material properties.[8] In pheomelanin, 1,4-benzothiazine (BTZ) derivatives are considered central intermediates that determine material properties, akin to the role of DHI in eumelanin;[9–11] however, compared to the information available for DHI/eumelanin, the structure–property relationship of BTZ in pheomelanin remains much less understood.

It is notable that eumelanin-like materials have found broad utility—ranging from ultraviolet (UV) shielding,[12–14] photothermal therapy,[15–17] photocatalysis,[18,19] to structural coloration,[20,21]—suggesting that subtle control of their molecular and supramolecular structures can translate into functional performance.[22–24] Beyond these applications, the inherent redox activity and π-conjugated framework of melanin have recently positioned these polymers as promising candidates for electrocatalysis, particularly the water splitting reaction.[25–27] While nitrogen doping is a common strategy to improve performance, single nitrogen-doping characteristic of eumelanin-like systems has shown limitations in significantly boosting catalytic efficiency. Recent studies have demonstrated that the introduction of secondary heteroatoms, particularly sulfur, provides a significantly greater promotional effect on electrocatalytic performance compared to nitrogen alone.[28] However, traditional eumelanin-like materials often encounter limitations in this context, such as suboptimal charge-transfer kinetics or a lack of long-range electronic order, which can hinder their overall efficiency. Guided by the need to overcome these challenges, we hypothesized that perturbing the BTZ pathway could yield pheomelanin-like films with interfacial electronic structures favorable for water oxidation. Among various options to perturb the BTZ pathway, we selected L-cysteine methyl ester (CME) and L-cysteine ethyl ester (CEE) for two primary reasons at the chemical level: (i) esterification retains the carboxylate group and thus inhibits decarboxylation that often drives aromatization in BTZ derivatives. By analogy to the case of DHI, carboxylation of BTZ derivatives is expected to

[a]*Department of Applied Chemistry, Kyung Hee University, Yongin, Gyeonggi 17104, Republic of Korea. E-mail: minhlee@khu.ac.kr; kkang@khu.ac.kr; minho.kim@khu.ac.kr*

[b]*School of Chemical Engineering, Sungkyunkwan University (SKKU), Suwon, 16419, Republic of Korea*

† These authors contributed equally to this work.

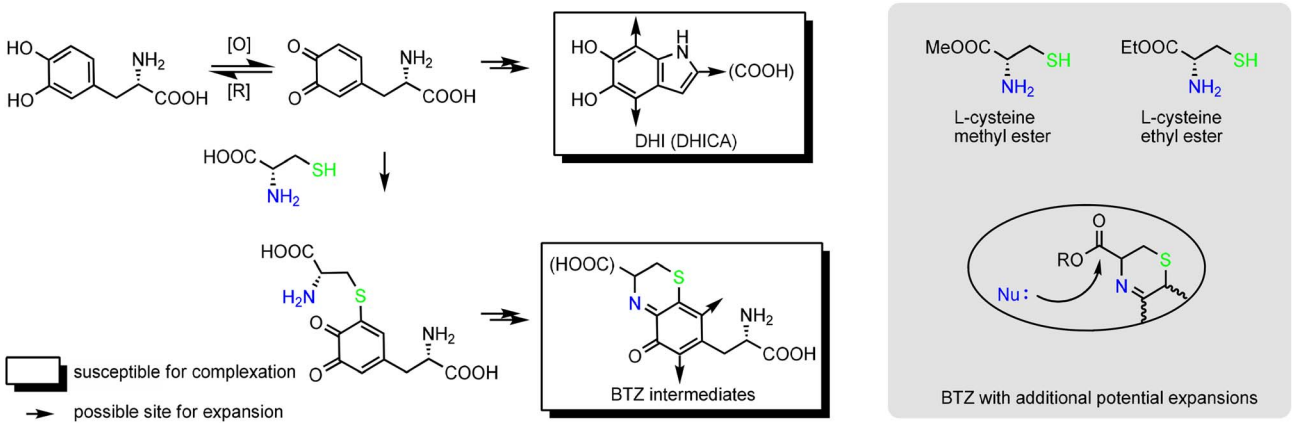

Fig. 1 Formation of DHI and BTZ that self-associate to form eumelanin and pheomelanin, respectively. Addition of CME or CEE leads to the formation of BTZ derivatives that may be nucleophilically expanded.

curb excessive inter-unit conjugation and tune the population of embedded radicals.[6,7] (ii) The ester carbonyl introduces an additional electrophilic site, enabling broader condensation and ring-expansion routes for BTZ-like intermediates. Taken together, these two design elements increase the structural diversity and the modes of self-association of BTZ units (π–π stacked or complexed assemblies), which we hypothesized would yield ultrasmooth, ultrathin pheomelanin-like films optimal for the oxygen-evolution reaction (OER) electrocatalysis.

Currently known high-performance electrocatalysts for water oxidation are mostly metal-based and, when scaled, often entail issues related to cost, scarcity, and environmental footprint.[29] The discovery of an organic, metal-free interfacial enhancer that can lower the overpotential and improve kinetics on conventional oxide anodes would therefore be beneficial for sustainable and economically viable hydrogen production.[30] Despite extensive studies on catecholamine coatings, most studies have focused on polydopamine (pDA) as a universal adhesive layer. Systematic exploration of pheomelanin-like coatings *via* BTZ-pathway engineering—and their implications for electrocatalysis—has remained limited.

It is worth noting that our use of CME and CEE is intended to enrich the diversity of BTZ-type intermediates and their supramolecular associations during film formation, rather than to introduce a specific functional group into the final complex polymer. This approach differs from conventional "functional-group grafting" strategies and instead aligns with methodologies aimed at studying or regulating complex systems. Guided by these assumptions, we set out to test whether CME/CEE-assisted deposition could produce conformal (~2 nm-thick) pheomelanin-like films on RuO_2 and deliver measurable enhancement in OER metrics compared to pDA or unmodified coatings.

Results and discussion

Non-linear increase in light absorption

Cysteine and its derivatives can react with various oxidized intermediates of dopamine (DA) or L-dopa in the process of melanogenesis. Under physiological and slightly basic conditions, a significant portion of thiols are deprotonated and can therefore react with oxidized quinone structures. In addition, thiols are readily oxidized to form disulfides in the presence of oxidants and often significantly slow the oxidative polymerization of catecholamines. Accordingly, the addition of cysteine was anticipated to significantly inhibit the deposition of pDA films, and efforts to design pheomelanin-like films have seldom been attempted.

Reflecting the formation of melanin-like materials, an aqueous solution of DA spontaneously exhibits a gradual, monotonic increase in light absorption across a broad range from UV to near-infrared (IR) regions—a trend often used as a hallmark of synthetic progression. As expected, this increase in light absorption was largely suppressed by the addition of the same molar concentration of CME (Fig. 2a). Under this condition, the color of the solution remained nearly unchanged for up to 48 h, whereas the basic DA solution without CME turned dark within approximately 1 h (Fig. S1). However, when the relative quantity of CME to DA was decreased ([DA] : [CME] = 10 : 2 mM), the solution showed an abrupt increase in light absorption over a broad wavelength range after a long (~30 h) quiescent period—hereafter referred to as a "burst" (Fig. 2b). In the short-wavelength region, the diluted samples showed that the ~280 nm band changed only modestly over the course of the reaction (Fig. S2). While the absorption feature near ~280 nm is commonly associated with π–π* transitions of the aromatic/catechol motif of DA, similar near-UV features can also persist in DA-derived oxidation products and oligomeric species during polymerization. In contrast, the featureless broadband absorption in the visible region is more specifically attributed to the emergence of extended conjugation, electronic coupling (including excitonic interactions), and aggregation-induced electronic states among DA-derived oligomers and higher-order assemblies.[31] Accordingly, the formation of a melanin-like material can undergo a kinetic transition manifested as a pronounced increase in visible absorption—even when the ~280 nm band changes only modestly and thus does not serve as a quantitative proxy for the concentration of the free DA

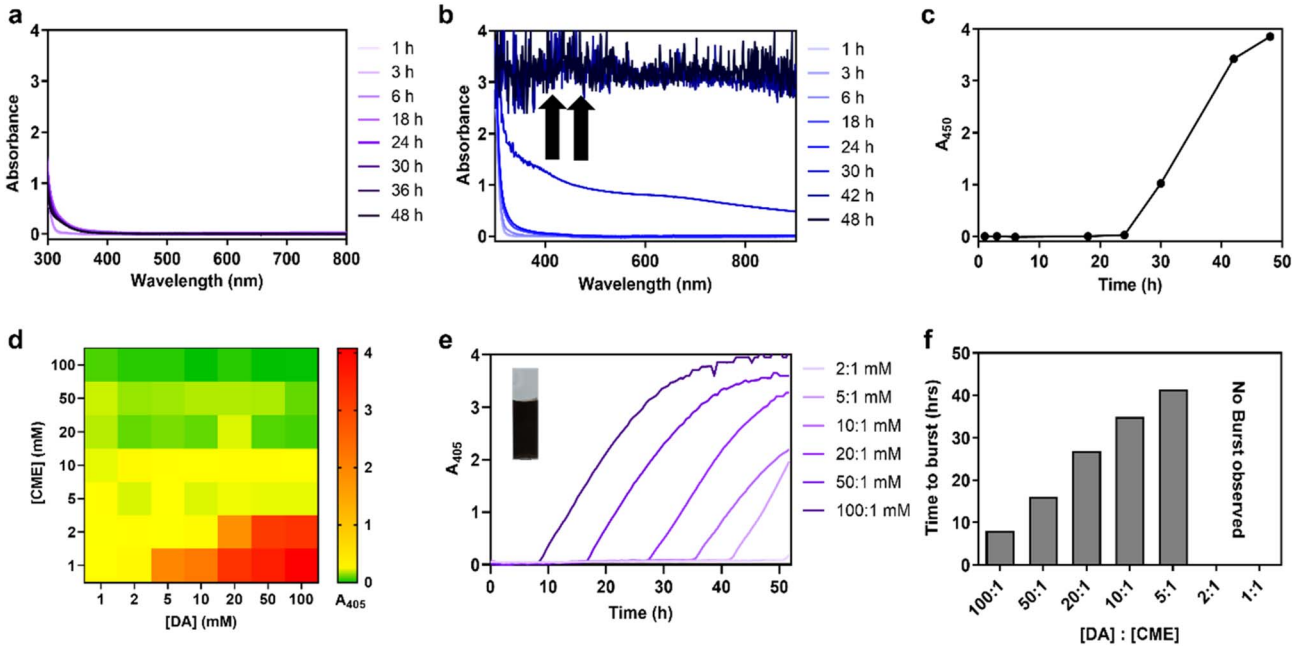

Fig. 2 UV-vis spectra and kinetics of DA + CME solutions under bursting and non-bursting conditions. (a and b) Time-dependent UV-vis spectra of solutions of DA + CME under (a) non-bursting conditions ([DA] : [CME] = 10 : 10 mM) and (b) bursting conditions ([DA] : [CME] = 10 : 2 mM). (c) Temporal increase of the A_{450} value, monitored to track the burst kinetics, of a solution under bursting conditions in (b). (d) Heat map presentation of A_{405} values, a representative wavelength of the high-energy region of the broadband absorption, of solutions with various ratios of [DA] and [CME] at 52 h. (e) Temporal changes of A_{405} values and (f) the time points when a burst was first observed for different ratios of [DA] and [CME]. (The inset in (e)) A photo of a mixed solution of DA + CME ([DA]:[CME] = 10 : 2 mM).

monomer. The burst occurred within a remarkably short period, in contrast to the preceding quiescent phase, and was accompanied by dramatic darkening of the solution (Fig. 2c and S3). To quantitatively track this abrupt optical transition, absorbance changes were monitored at selected wavelengths within the high-energy visible region. Melanin-like materials are known to exhibit featureless, broadband absorption that increases monotonically toward shorter wavelengths (~400–500 nm) as aggregation and excitonic broadening progress, rather than showing discrete molecular absorption bands.[32] Accordingly, absorbance at 450 nm was used for time-resolved analysis of the burst behavior shown in Fig. 2c, as this wavelength lies within the broadband absorption regime while providing a wide dynamic range, improved signal-to-noise ratio, and reduced risk of early signal saturation under our experimental conditions. This kinetic trend is a characteristic of a non-linear chemical process, likely involving an autocatalytic component. The presence of a quiescent period implies that the burst may occur only after CME is depleted or rendered redox-inactive through the reaction with oxidized DA species. This hypothesis is further supported by nuclear magnetic resonance spectroscopy (NMR), showing depletion of cysteine esters over time (Fig. S4). These findings also imply that the material—whether in solution or deposited on a surface—likely differs in composition and structure before and after the burst event.

We next investigated whether the onset of the burst is determined by the ratio between DA and cysteine esters by comparing solutions with different molar ratios of DA and CME or CEE in a microwell plate. For systematic comparison under a large number of conditions in the microwell-plate experiments, absorbance at 405 nm was monitored as a representative wavelength in the high-energy region of the broadband absorption, which reflects the extent of melanin-like material formation and has been widely used as a proxy for aggregation-driven optical evolution in melanin systems.[32] When the amount of cysteine ester was comparable to that of DA (*e.g.*, a molar ratio of 1 : 1 or 2 : 1 for DA/CME or DA/CEE), no burst was observable over an extended period (>52 h; Fig. 2d, S5, and Table S1). When the concentration of DA was fixed, increasing the molar ratio of DA : CME resulted in a slower onset of the burst in an approximately linear fashion (Fig. 2e and f), again implying that the burst is correlated with depletion of CME in solution. When a burst took place, the solution concurrently darkened and became enriched with insoluble species, similar to what occurs—albeit much earlier—in a DA-only solution (Fig. 2e, inset). We note that the onset times measured in the microwell-plate experiments were substantially delayed relative to those measured under the same conditions using glass vials (Fig. S6). It is known that the kinetic parameters governing the formation of pDA depend critically on the reaction container.[33] Nonetheless, experiments conducted within the same container still provide internally consistent and tractable kinetic information, as demonstrated by the results obtained using a microwell plate presented above. Reproducibility of the microwell-based reactions was further confirmed through repeated measurements (Fig. S7). Differences between CME and CEE were minimal with respect to their ability to regulate the burst, whereas cysteine itself behaved distinctly from both ester

derivatives (Fig. S8). This observation suggests that esterification of the carboxylic group plays a critical role in determining how cysteine derivatives influence pDA formation.

Deposition of pheomelanin-like films

Melanin-like materials, including pDA, are widely regarded as disordered, graphene- or graphite-like amorphous organic networks.[34,35] Their structures are commonly described in terms of heterogeneous π-conjugated domains, defective graphitic motifs, and edge-rich carbon and nitrogen functionalities, which collectively govern optical absorption, redox activity, and interfacial charge transport. Within this general framework, variations in precursor chemistry and reaction pathways are known to modulate the local bonding environments and supramolecular organization of these graphitic-like networks, thereby giving rise to distinct deposition behaviors and interfacial properties. In this context, we next examined how the introduction of cysteine ester derivatives alters the deposition behavior and interfacial manifestation of melanin-like films formed from DA under basic conditions.

The darkening of a basic DA solution is generally correlated with the deposition of a pDA film at solid–liquid and air–liquid interfaces. pDA film formation relies primarily—but not exclusively—on the sedimentation of covalently and noncovalently crosslinked oligomeric species, which normally exhibit strong light absorption. The solution darkens as DA-derived oligomeric species grow in size, and larger oligomers are more likely to sediment and form an organic film. Since the addition of cysteine esters significantly attenuated darkening of the solution, we initially anticipated that it would prevent the deposition of the pDA film. However, we unexpectedly observed an evident change in the wettability of a gold substrate that had been in contact with a transparent solution of DA and CME or CEE (*i.e.*, before a burst), indicating a remarkable change in the

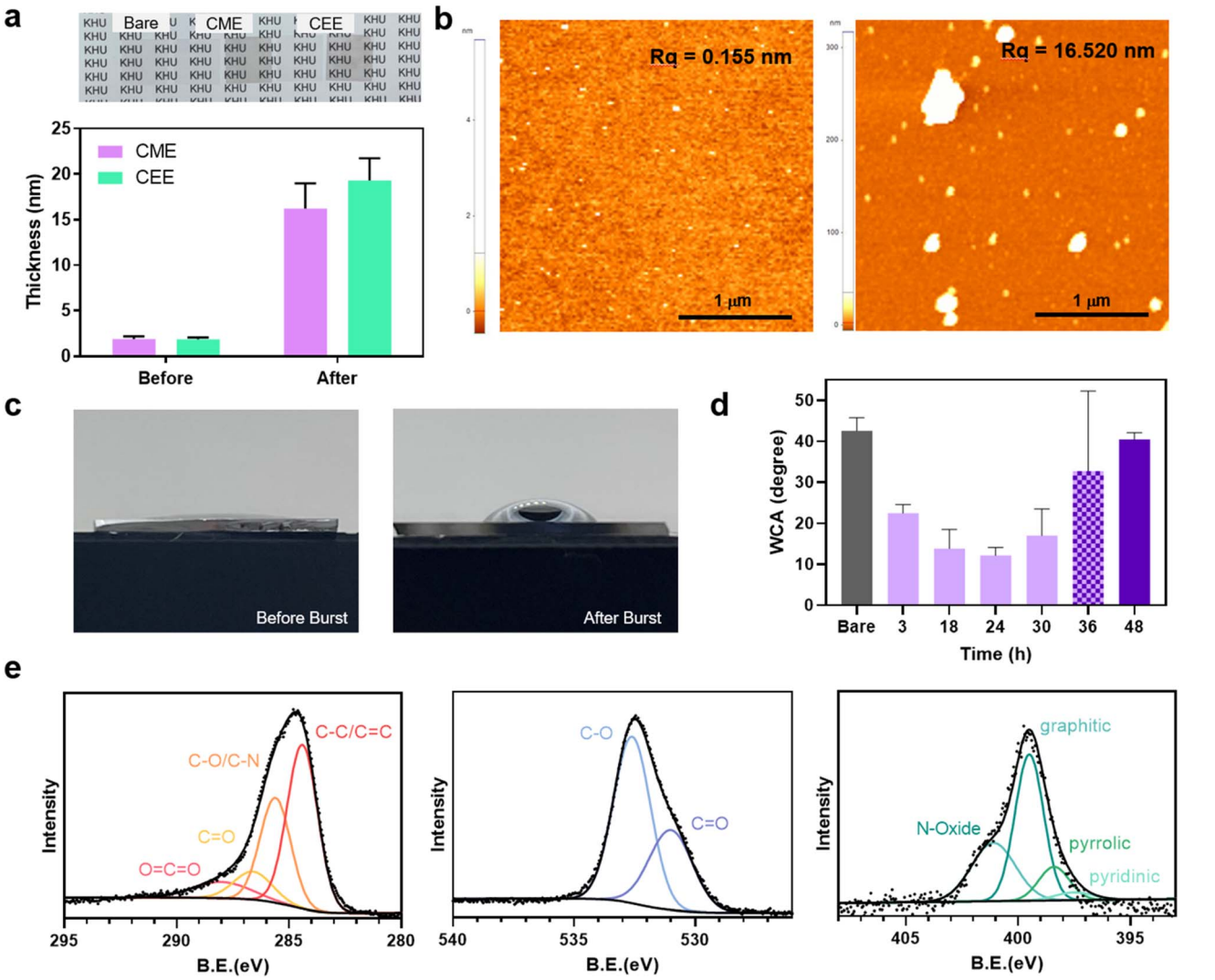

Fig. 3 Film characterization before and after burst: morphology, thickness, wettability, and chemical composition. (a) Photos of the films coated on glass substrates after burst (48 h deposition) and the thickness of the films coated on Si wafers before (18 h) and after (48 h) burst. (b) AFM images and (c) photos of a water droplet on the CME films before (left) and after (right) burst. (d) Time-dependent evolution of water contact angle with increasing deposition time. (e) XPS spectra of a film coated before burst. (Burst conditions; [DA] : [CXE] = 10 : 2 mM).

chemical structure of the surface. To further characterize this, silicon wafer substrates were immersed in the solution of DA and cysteine ester. Up to 18 h of incubation—during which no burst occurred—the substrate showed negligible color changes (Fig. 3a). Nonetheless, ellipsometric measurements clearly indicated the presence of an organic thin film growing very slowly (Fig. 3a). After 18 hours, the film reached only ~2–3 nm in thickness, in stark contrast to the standard method of pDA deposition, which typically yields ~100 nm-thick films over the same duration.[36] Thin film formation was detectable even within the first 2 h of incubation, after which no substantial growth occurred until the burst took place (Fig. S9). After 36 h (*i.e.*, post-burst), we observed abrupt film growth, reaching 16.20 ± 2.80 nm and 19.30 ± 2.44 nm for CME and CEE, respectively, at 48 h. This abrupt growth coincided with a visible color change on the substrates (Fig. 3a). A similar trend was observed on gold substrates, indicating that the deposition of a thin film may occur on various types of substrates (Fig. S10). This initial transparent layer shares functional similarities with the early, non-pigmented stage of traditional alkaline pDA formation, which is characterized by stable interfacial anchoring and high wettability. While this stage is typically a transient precursor to rapid nanoaggregation, the cysteine esters effectively 'stall' the polymerization, maintaining an ultrathin interface for an extended period. The subsequent 'burst' in growth is triggered only upon the depletion of these chemical modulators (Fig. S4), at which point the system transitions into the rapid, aggregate-driven deposition characteristic of mature melanin-like materials.

Atomic force microscopy (AFM) analysis showed that the morphologies of films deposited before and after the burst differ dramatically (Fig. 3b and S11). Films deposited under non-bursting conditions exhibited extremely smooth morphologies without irregular features. The burst, on the other hand, led to the formation of films containing spherical sediments, similar to those observed in conventional pDA or other melanin-like films. Consistent with this distinction, roughness values extracted from AFM images obtained under non-bursting conditions were substantially lower than those measured under bursting conditions.

The film deposited under non-bursting conditions was abnormally thin, and its morphology was barely distinguishable from that of the bare substrate. Notably, it nonetheless showed a remarkable change in water wettability. Substrates immersed in a non-bursting DA + CME solution exhibited an extremely high degree of hydrophilicity to the extent that a stable droplet could not be formed for contact angle measurement (Fig. 3c). As the film grew thicker after the burst, the hydrophilicity of the substrates markedly decreased, with water contact angles increasing to 41.82 ± 2.18° (Fig. 3c, d, and S12). It is notable that this value is comparable to those typically measured for conventional pDA films,[37] implying that the film formed under bursting conditions more closely resembles pDA than that deposited before the burst. To further examine the chemical nature of these films, we conducted X-ray photoelectron spectroscopy (XPS) analyses on the films deposited under bursting conditions. The atomic composition of the film was measured to be 65.34, 7.77, and 19.83% for C, N, and O, respectively. The C 1s, N 1s, and O 1s spectra indicated that the films were primarily composed of C–C/C=C, C–O/C–N, pyrrolic N, and graphitic N species (Fig. 3e, S13 and S14). The presence of graphitic N was particularly notable, as it is absent from the oligomeric intermediates typically formed during the polymerization of pheomelanin or melanin. In addition, the S 2p spectrum of the burst-stage film exhibited a characteristic doublet corresponding to S $2p_{3/2}$ and S $2p_{1/2}$, with the S $2p_{3/2}$ component appearing slightly more intense, consistent with the expected spin–orbit splitting of sulfur species (Fig. S14c).[38] These results confirm the incorporation of sulfur-containing moieties within the melanin-like film.

To further elucidate the chemical nature of the films formed before and after the burst, as well as their distinction from conventional pDA, we performed solid-state ^{13}C cross-polarization total suppression of sideband (CP-TOSS) NMR analyses on the bulk materials prepared under corresponding conditions (Fig. S15). Unlike surface-sensitive techniques, solid-state NMR probes the averaged chemical environments within the entire organic network and is therefore well suited to assess whether cysteine ester derivatives are chemically incorporated into the melanin-like framework.

The ^{13}C CP-TOSS spectra of CME- and CEE-derived materials exhibited dominant broad resonances in the aromatic region (approximately 110–150 ppm), consistent with the formation of heterogeneous π-conjugated melanin-like networks. Importantly, both CME and CEE samples displayed pronounced carbonyl signals near ~170 ppm, along with ester-specific alkoxy resonances that were absent from pDA. In particular, the CME-derived sample showed a characteristic resonance at ~51 ppm, assignable to the O–CH_3 group of a methyl ester, while the CEE-derived sample exhibited distinct resonances at ~71 ppm (O–CH_2) and ~16 ppm (CH_3), consistent with ethyl ester moieties.

In contrast, the ^{13}C CP-TOSS spectrum of pDA was dominated by broad aromatic (110–150 ppm) and aliphatic (30–45 ppm) resonances, without discernible ester-related features. Moreover, all spectra were characterized by broad signals rather than sharp monomer-like peaks, indicating polymerized, chemically heterogeneous solids rather than residual low-molecular-weight species. Raman spectroscopy and liquid chromatography-mass spectrometry (LC-MS) analysis also corroborated these findings, identifying distinct structural fingerprints and molecular intermediates unique to the pre-burst phase (Fig. S16). LC-MS analysis was performed on aliquots taken from the DA + CXE reaction solution prior to the onset of the burst event. The ESI+/MS spectra revealed molecular ion peaks corresponding to intermediates consistent with BTZ-based derivatives, suggesting the formation of sulfur-containing melanin-like intermediates during the pre-burst stage. Raman spectroscopy was carried out on the powder samples obtained immediately after the burst event, where sufficient solid material could be collected for spectroscopic analysis. The resulting spectra were largely dominated by features characteristic of eumelanin-like structures. To further probe the potential formation of pheomelanin-like species, the fingerprint regions at 500–550 cm^{-1} and 700–750 cm^{-1}—assigned to C–S vibrational modes and BTZ ring vibrations, respectively—were examined in

an enlarged view. Weak but discernible signals were observed within these regions, indicating the presence of structural motifs consistent with pheomelanin-like components. However, it is important to note that the definitive identification of specific BTZ-related motifs remains a profound analytical challenge due to the intrinsic chemical heterogeneity and disordered amorphous nature of melanin-like polymers. Such structural complexity typically results in broad, overlapping spectral features that obscure distinct molecular signatures, which account for the scarcity of direct evidence for these motifs in prior literature. Consequently, the convergence of our multi-modal analytical findings provides a self-consistent and compelling indication of the activation of the pheomelanin-like chemical pathway. Taken together, the analytical data suggest that the non-bursting CME- and CEE-derived films are chemically distinct from conventional pDA, and that the ultrathin films formed prior to the burst already possess a unique sulfur-containing melanin-like chemical microstructure.

Application of CME and CEE films in OER electrocatalysis

Because melanin-like materials are organic, they exhibit conductivity only under specific conditions, making the formation of uniform, nanometer-scale films essential for reliable transfer of electrons and protons. Traditional pDA films have often struggled to achieve such uniformity, thereby compromising conductivity. In contrast, the CME- and CEE-based methodologies enable precise control over the production of exceptionally thin and uniform coatings, as evidenced by transmission electron microscopy (TEM) in Fig. 4a and b.

To evaluate the electron-transfer capabilities of these melanin-like films, their charge transfer kinetics were assessed using the OER as a benchmark. CME, CEE, and pDA films were deposited onto RuO_2 particles—a benchmark OER catalyst—yielding RuO_2@CME, RuO_2@CEE, and RuO_2@pDA, respectively. TEM analysis revealed that CME- and CEE-derived films, each approximately 2 nm thick, provided uniform and conformal coatings on the RuO_2 particles (Fig. 4a and b). Notably, both RuO_2@CME and RuO_2@CEE exhibited improved OER performance compared to pristine RuO_2 as demonstrated by linear sweep voltammetry (LSV) curves measured in 1 M KOH. Specifically, the overpotentials at a current density of 10 mA cm^{-2} (η_{10}) decreased to 293 mV and 315 mV for RuO_2@CME and RuO_2@CEE, respectively, compared with 327 mV for pristine RuO_2 (Fig. 4c). This trend became even more pronounced at a higher current density of 100 mA cm^{-2} (η_{100}), with overpotentials of 364 mV, 406 mV, and 503 mV for RuO_2@CME, RuO_2@CEE, and pristine RuO_2, respectively. In contrast, RuO_2@pDA exhibited reduced OER performance compared to pristine RuO_2, likely due to its thicker melanin-like film impeding charge transfer. Tafel plots derived from the LSV results were analyzed to further evaluate the electrochemical catalytic kinetics of RuO_2@CME, RuO_2@CEE, and pristine RuO_2 (Fig. 4d). RuO_2@CME exhibited the lowest Tafel slope of 68.4 mV dec^{-1}, indicating superior kinetics, while RuO_2@CEE, RuO_2@pDA, and pristine RuO_2 showed higher Tafel values of 82.1, 156.5, and 113.7 mV dec^{-1}, respectively. These results suggest that enhanced reaction kinetics lead to reduced overpotentials in both RuO_2@CME and RuO_2@CEE, while the pDA coating inhibits catalytic activity. Additionally, charge transfer resistance (R_{ct}) values derived from electrochemical impedance spectroscopy (EIS) further confirmed the trend in electrocatalytic performance (Fig. 4e). The R_{ct} values were significantly lower for RuO_2@CME (21.6 Ω) and RuO_2@CEE (36.3 Ω) than for RuO_2@pDA (81.2 Ω) and pristine RuO_2 (73.8 Ω). These results indicate that the choice of the melanin-like film on RuO_2 enables control over charge transfer kinetics, thereby directly influencing catalytic activity for the OER. The detrimental effect of pDA is attributed to its thick, capacitive organic film. The long-term stability of the best performing catalysts, RuO_2@CME and RuO_2@CEE, was evaluated *via* chronopotentiometry at 10 mA cm^{-2}. Both catalysts retained stable OER performance over 10 h without significant potential drift (Fig. 4f).

To further ensure that the observed enhancement in OER activity is not solely attributable to differences in the film thickness, thinner pDA films (~10 nm) were prepared by lowering the deposition time under alkaline conditions, alongside thicker pDA coatings fabricated under otherwise identical conditions (Fig. S17). While the CME- and CEE-derived coatings exhibited ultrathin thicknesses on the order of ~2 nm, continuous and uniform pDA films could only be reliably formed down to approximately 10 nm (Table S2).[39–44] The inherent difficulty in achieving reproducible, ultra-thin thickness (<10 nm) *via* traditional alkaline deposition (typically at pH ~8.5) is fundamentally rooted in the rapid auto-oxidation and polymerization kinetics of dopamine. In these high-pH environments, the thermodynamic driving force is so high that the stages of primary nucleation and subsequent oligomer aggregation overlap significantly. This results in a deposition process that is difficult to terminate precisely at the sub-10 nm scale without compromising surface uniformity.

Within this set of thickness-controlled pDA samples, the reduced-thickness pDA coatings exhibited electrocatalytic activity comparable to that of bare RuO_2, indicating that pDA films at this thickness do not intrinsically suppress the activity of the underlying RuO_2 substrate (Fig. 4c–e). Specifically, the thin pDA-coated RuO_2 showed an η_{10} of 315.6 mV and a Tafel slope of 117.8 mV dec^{-1}, both of which are close to the values obtained for pristine RuO_2. The η_{100} increased to 447.8 mV, reflecting limited charge-transfer capability under high-rate operating conditions. EIS measurements further revealed that even the reduced-thickness pDA films exhibited a relatively high R_{ct} of 79.4 Ω, comparable to that of bare RuO_2 and substantially higher than those of the CME- and CEE-derived films.

As an additional control experiment to probe the chemical origin of the enhanced activity, we prepared RuO_2 catalysts coated with melanin-like films derived from non-esterified cysteine under comparable conditions. Despite the presence of thiol functionality, the cysteine-derived coatings exhibited significantly lower OER activity than their CME- and CEE-derived counterparts (Fig. S18), indicating that thiol groups alone are insufficient to impart enhanced electrocatalytic performance.

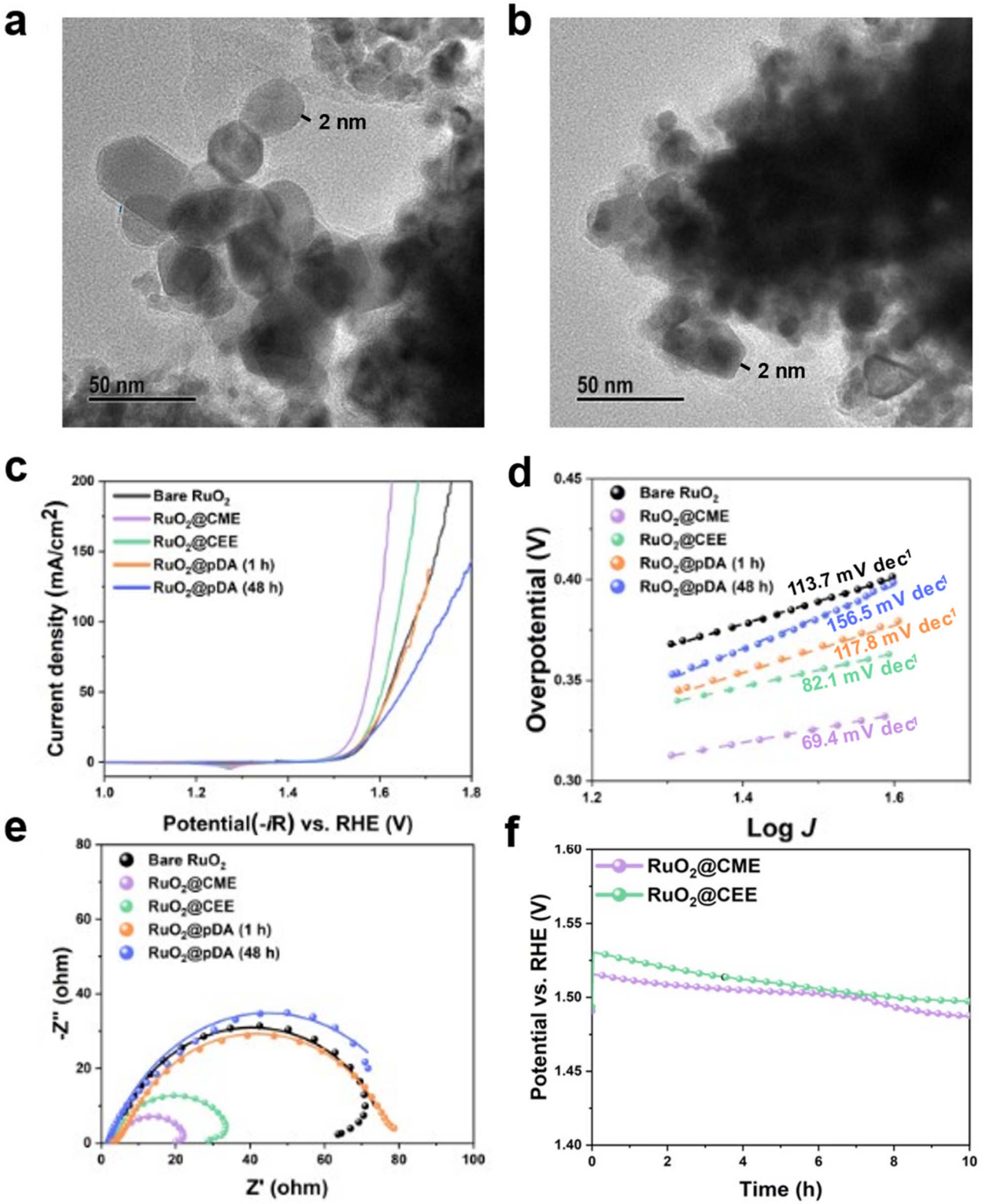

Fig. 4 TEM images and electrochemical analyses. (a and b) TEM images of RuO_2@CME and RuO_2@CEE, respectively. (c) LSV curves, (d) Tafel plots, and (e) Nyquist plots for bare RuO_2, RuO_2@CME, RuO_2@CEE, RuO_2@pDA (1 h), and RuO_2@pDA (48 h). (f) Chronopotentiometry curves of RuO_2@CME and RuO_2@CEE. RuO_2@CXE denotes RuO_2 particles coated by immersion in an aqueous solution containing dopamine and CXE.

This result highlights the critical role of esterification in defining the chemical microstructure and interfacial properties of cysteine-derived melanin-like films. Esterification of the carboxyl group is expected to modulate hydrogen-bonding interactions, molecular packing, and electronic coupling within the film, thereby enabling more efficient charge transfer across the catalyst–electrolyte interface. Taken together with the thickness-controlled pDA experiments, these findings demonstrate that the superior OER activity of CME- and CEE-coated RuO_2 arises from their unique chemical characteristics imparted by the esterified cysteine derivatives, rather than from the film thickness or the mere presence of thiol functionality.

Theoretical rationalization of the facilitating role of the pheomelanin-like film in the OER

To shed light on the potential mechanism by which the ultrathin pheomelanin-like film facilitates the OER, density functional theory (DFT) calculations were performed using the CME-derived structural model proposed in Fig. 5a. At present, we cannot unambiguously confirm or exclude the formation of discrete DHI/DHICA motifs under CME/CEE-assisted conditions, because the resulting melanin-like films are chemically heterogeneous and lack unique, diagnostic spectroscopic signatures. Accordingly, we discuss the reaction pathway in terms of kinetically plausible quinone trapping and subsequent coupling processes. Previous studies have shown that the OER activity of graphitic carbon atoms can be controlled by both edge effects and electrophilicity, wherein carbon atoms that are more positively charged and located near the edge of graphene exhibit stronger adsorption of OER intermediates.[45] In particular, both formation and activation of the *O intermediate are critical for efficient OER on graphene-based materials.[46] While a carbon-based graphene structure typically favors epoxide intermediates, electronic modulation of the graphitic layer can shift the reaction preference toward the formation of enolate intermediates.[47] In the structural model proposed in this work, resonant tautomers alter the active imine carbon sites and their electrophilicity through the involvement of graphitic and edge N atoms (Fig. 5b). The development of graphitic nitrogen distinguishes the preferred tautomeric states—adjacent imine sites (*e.g.*, C_{10}) favor a keto-imine tautomer without graphitic N, while nonadjacent edge imine sites favor an enamine tautomer with graphitic N. This distinction arises from the presence of graphitic N, which stabilizes a distinct tautomeric structure to reduce formal charge separation.

Coupled with OER thermodynamic analysis, the Mulliken charge data reveal a strong correlation between the electrophilicity of a carbon atom and the stability of *OH and *OOH intermediates in the graphitic structure (Fig. S19). As previously reported,[45] a more positive Mulliken charge on a carbon atom enhances the adsorption strength of OER intermediates at graphitic carbon sites. However, edge carbon atoms show a reversed trend that more electron-rich carbons (*e.g.*, C_5) show stronger adsorption of *OH and *OOH, indicating that adsorption preferences at edge carbon sites are governed primarily by edge effects rather than electrophilicity. Mulliken charge analysis in Fig. 5c further highlights this distinction, showing that carbon atoms adjacent to graphitic N are relatively electron-poor (+0.35e) in contrast to edge carbon atoms, which are more electron-rich (+0.23 to −0.01e). Based on these charge distributions, the epoxide intermediates preferentially form at the edge imine sites (C_1, C_5, C_6, C_7, and C_9), while enolate intermediates are stabilized at the most electron-poor carbon sites (C_3 with +0.54e and C_{10} with +0.36e).

As shown in the overall OER thermodynamic profiles in Fig. 5d and S20, the most active OER site in the structure without graphitic N is the edge imine carbon (C_{10}), where a bridged *O atom is adsorbed over an imine N=C bond. However, the allylic carbon (C_2) shows excessively strong adsorption of *O in the form of an epoxide (−1.03 eV), resulting in an unacceptably high activation barrier for *OOH formation (+1.81 eV) (Fig. S20a). In the graphitic structure, a higher population of edge imine becomes accessible. For example, the imine-bridged *O intermediate at the C_7 site shows moderately improved stability (+0.58 eV) compared to its counterpart in the non-graphitic N (+0.64 eV), revealing the thermodynamic advantage of edge effects in a graphitic structure. On the other hand, the imine carbon adjacent to the central N (C_{10}) can adsorb an enolate intermediate due to its high electrophilicity. However, the enolate is overly stabilized (−0.30 eV), leading to a large activation barrier for conversion to *OOH (+1.32 eV) (Fig. S20b). Therefore, optimal OER activity can be achieved by a balance between *O formation and activation, particularly at edge imine carbon atoms. The correlation plot showing *O formation energy (ΔG_2, $*OH + OH^- \rightarrow *O + H_2O + e^-$) *versus* *O activation energy (ΔG_3, $*O + OH^- \rightarrow *OOH + e^-$) displays a negative correlation between the two parameters. Among all sites analyzed, C_7 with graphitic N exhibits the most favorable balance between activity and stability for the *O intermediate, outperforming C_{10} in the structure without graphitic N (Fig. 5e). Overall, the graphitic structure maximizes both OER activity and the population of the catalytically active edge imine carbon atoms, while graphitic N contributes to the stability of intermediates *via* resonance effects.

The significance of specific functional groups in the film structures was estimated through charge difference analysis and interfacial interaction energy calculations (Fig. S21). Bader charge analysis and charge density differences reveal that increasing the film thickness by the adsorption of additional layers significantly reduces charge transfer efficiency, regardless of the molecular structures of the film (from +1.10e to +0.25e for CME and from +1.28e to +0.28e for pDA). However, the main difference lies in the atomic contributions to the interfacial interactions. The interaction between RuO_2 and pDA molecular units is dominated by localized hydrogen bonding, whereas CME exhibits a more uniformly distributed charge density difference across the heteroatoms of its aromatic rings in the secondary CME. This contrast indicates that esterified organic moieties without hydrogen bonding can more effectively and homogeneously modulate the electronic properties of the film through interfacial charge redistribution.

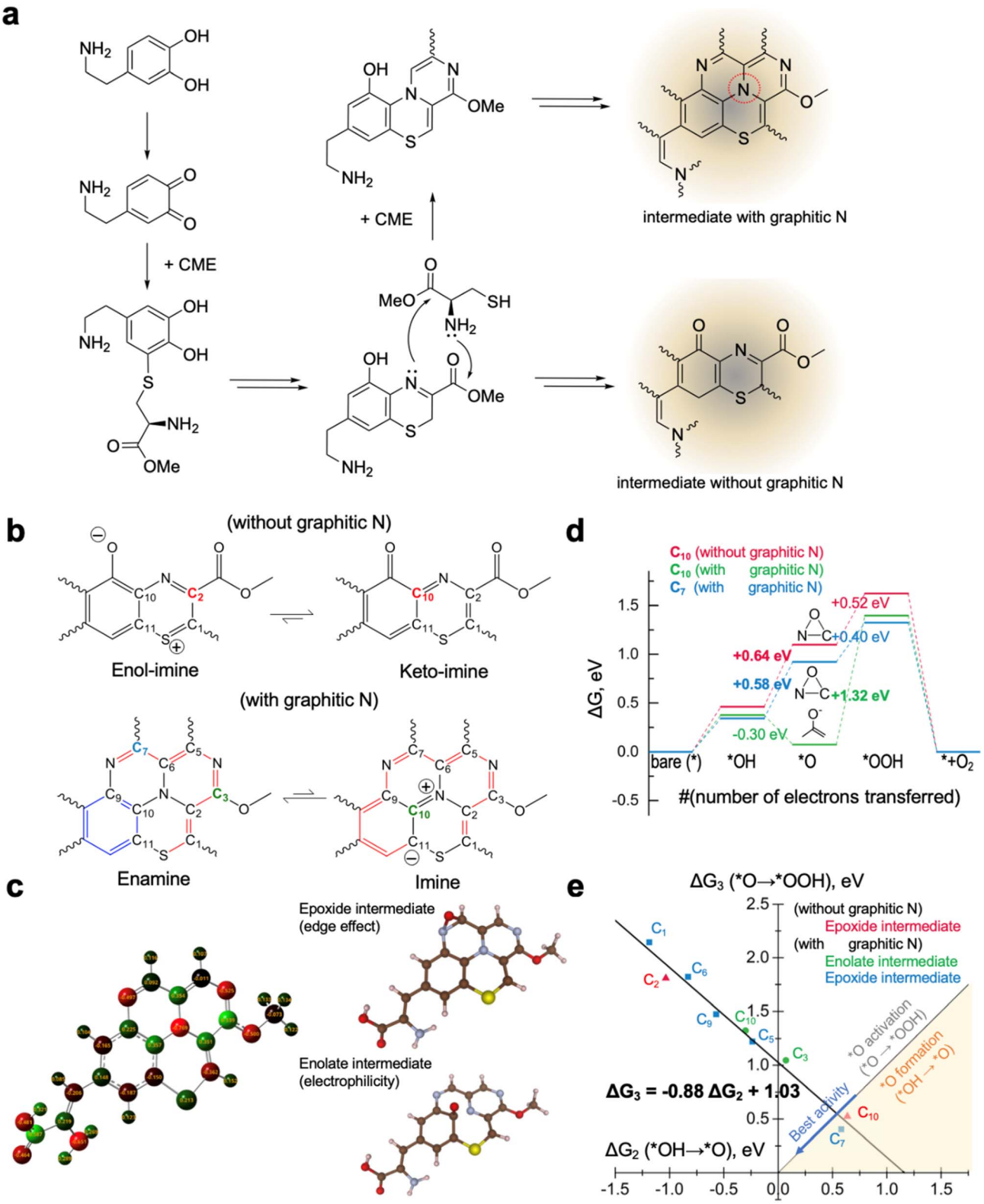

Fig. 5 Theoretical analysis of oxygen evolution thermodynamics and potential determining steps with and without graphitic N. (a) Possible pathways of the formation of intermediates with and without graphitic N. (b) Resonance structures of the CME derivative (top) without and (bottom) with graphitic N, (c) Mulliken charge and *O intermediates in the epoxide structure at the edge carbon (C_7) and the enolate structure at the carbon adjacent to the graphitic N (C_{10}), and (d) Gibbs free energy diagram of OER electrocatalysis occurring before the graphitic growth at C_{10} (red) and after the graphitic growth at C_{10} (green) and at C_7 (blue). (e) correlation plot of free energy change of *O formation, ΔG_2 (*OH → *O, *x* axis), and *O activation, ΔG_3 (*O → *OOH, *y* axis). The yellow region includes the carbon sites whose potential determining step is *O formation, and the other region indicates that the potential determining step is *O activation.

Conclusions

While traditional chemical design favors simple and predictable molecular compositions, complex systems leverage compositional diversity to manifest emergent properties such as adaptation and spontaneous organization. By embracing this complexity through the BTZ-based pathway, we demonstrate a practical strategy for realizing emergent material functions—specifically optimized interfacial electronic structures—that remain elusive in traditional, simplicity-rooted molecular regimes.

In this study, we investigated a catecholamine-derived complex system, building upon previously reported pheomelanin-inspired materials,[48–50] to harness emergent properties for enhancing electrocatalytic performance. Specifically, we demonstrated that a pheomelanin-like film—drawing inspiration from natural pigment chemistry—can serve as an effective bioinspired interfacial modifier to improve the OER on conventional metal-based catalysts. By introducing a thin, ultrasmooth organic layer, we achieved significant reductions in overpotential and improved charge transfer kinetics, highlighting the potential of organic–inorganic hybrid designs for catalysis. This bioinspired strategy offers a promising path toward more efficient and sustainable electrocatalytic systems, contributing to the advancement of renewable energy technologies such as large-scale hydrogen production.

Materials and methods

Materials

The following chemicals, DA hydrochloride, CME hydrochloride, CEE hydrochloride, and Tris(2-carboxyethyl)phosphine hydrochloride were purchased from Thermo Fisher Scientific. 1 M Tris–HCl, pH 8.5 was purchased from Biosesang (South Korea). RuO_2 was purchased from Sigma-Aldrich. All reagents were used without any further purification. Microscope slides (DU. 2355031) were purchased from Daihan Scientific (South Korea). Corning® 96-well black polystyrene microplates were purchased from Thermo Fisher Scientific.

Deposition of pheomelanin-like films

All substrates were cleaned by ultrasonication in distilled water, ethanol, and acetone for 15 min each, before being dried under N_2 flow. The cleaned substrates were immersed in 10 mM Tris–HCl buffer solutions (pH 8.5) with given concentrations of DA hydrochloride and CME/CEE under vigorous stirring at room temperature. After stirring, each substrate was washed with distilled water and dried under N_2 flow.

Coating of RuO_2 particles

0.30 mmol of RuO_2 particles were added to 10 mM Tris–HCl buffer solutions (pH 8.5) of DA hydrochloride and CME/CEE under vigorous stirring at room temperature. After a desired reaction time, the solution was centrifuged (15 000 rpm and 15 min) and washed with distilled water three times. After freeze-drying, the coated particles were used for further analysis.

Material characterization

The UV-vis absorbance spectra of the sample solutions were obtained using a Lambda 465 spectrophotometer (PerkinElmer, Inc., USA). Prior to each measurement, the containers were vortexed and sonicated for 10 s. For measuring light absorption at various reactant concentrations, a multifunctional microplate reader (FLUOstar OPTIMA, BMG Labtech, Germany) was used. The water contact angle was measured by dropping 5 μL of deionized water onto each sample, and the static angles were analyzed using ImageJ software. Spectroscopic ellipsometry (Elli-SE, Ellipso Technology, Suwon, South Korea) was performed over the wavelength range of 400–700 nm at an incidence angle of 70°. AFM imaging of the substrates was conducted using an atomic force microscope (XE-150, Park Systems, South Korea). An NCHR-50 AFM cantilever (NanoWorld, Switzerland) with a typical resonant frequency of 320 kHz and a force constant of 42 N m^{-1} was employed in non-contact mode to determine topographic profiles. The root-mean-square roughness (R_q) was calculated over a 5 × 5 μm^2 area. XPS spectra were obtained using K-Alpha (Thermo Electron) and Nexsa (ThermoFisher Scientific, USA) instruments with a 400 μm X-ray spot size. ^{1}H NMR spectra were recorded on a JNM-ECZ400S/L1(400 MHz) spectrometer. The samples were prepared with 10 mM DA hydrochloride and 2 mM CME/CEE in Tris-d_{11} buffer (pH 8.5) using D_2O dilution. Solid-state ^{13}C CP-TOSS NMR spectra were obtained using a 500 MHz Avance III HD (Bruker, USA) at the National Center for Inter-University Research Facilities (NCIRF) of Seoul National University. The samples were prepared with 10 mM DA hydrochloride and 2 mM CME/CEE in Tris buffer (10 mM, pH 8.5). Experiments were performed at 298 K. Each 1D^{13}C CP-TOSS spectrum was acquired under magic-angle spinning (MAS) at 5 kHz. The recycle delay was 3.0 s, and 5120 scans were accumulated for each spectrum. ^{13}C chemical shifts are reported in parts per million (ppm) and were referenced externally to ^{13}C glycine (176.4 ppm).

Electrochemical measurements

Electrochemical measurements were conducted using an SP300 electrochemical workstation (Bio-logic Science Instruments, France) in a standard three-electrode system with 1 M KOH as the electrolyte. A Hg/HgO electrode and a Pt mesh were used as the reference and counter electrodes, respectively. To evaluate the electrocatalytic activity of melanin-like species coated RuO_2, LSV was carried out at a sweep rate of 2 mV s^{-1}. EIS measurements were conducted at a constant bias of 0.7 V *vs.* Hg/HgO over a frequency range from 0.01 Hz to 100 000 Hz with an amplitude of 0.01 V. Chronopotentiometric measurements were performed at a constant current of 10 mA cm^{-2}. The potential of the working electrode was recalibrated to the reversible hydrogen electrode (RHE) using the following equation:

$$E_{RHE} = 0.098 + (0.0592 \times pH) + E_{Hg/HgO}$$

The overpotential (η) for the OER was determined by subtracting the theoretical potential for water oxidation (1.23 V) as follows:

$$\eta = E_{\mathrm{RHE}} - 1.23$$

Tafel slopes were derived from the polarization curves according to the Tafel equation:

$$\eta = a + b \log J$$

DFT calculations

Unrestricted density functional calculations were performed using Gaussian 16.[51] The unrestricted B3LYP exchange correlation functional[52] with the 6-31+G* basis set was chosen for all calculations. The intermediate structure was visualized using VESTA 3.5.7.[53] Vibrational frequencies were calculated for Gibbs free energy changes at 298.15 K. The polarizable continuum model with the integral equation formalism (IEFPCM) was employed for the aqueous solvent environment.[54] The chemical potential of the proton and electron was calculated using the computational hydrogen electrode model:[55]

$$\mu(\mathrm{H}^+) + \mu(\mathrm{e}^-) = \frac{1}{2}\mu\left(\mathrm{H}_{2(\mathrm{g})}\right) - \mathrm{e}U$$

The interaction between the RuO_2 (110) surface and molecular moieties in the films was investigated using the Vienna *ab initio* Simulation Package (VASP) 5.4.1.[56] The Perdew–Burke–Ernzerhof (PBE) exchange-correlation functional[57] was employed with Grimme's D3 dispersion correction.[58] The pseudopotentials were described based on the projector-augmented wave method,[59] with a kinetic energy cutoff of 400 eV. The Brillouin zone was sampled using a $(4 \times 2 \times 1)$ Monkhorst–Pack *k*-point mesh.[60] A vacuum region of 20 Å was applied normal to the RuO_2 surface. All structures were relaxed until the last energy differences reached 10^{-3} eV, while the bottom half of the RuO_2 slab was fixed during optimization. Bader charge analysis was performed using the code developed by Henkelman's group,[61] and charge density differences were visualized using VESTA 3.5.8.[53]

Author contributions

MHL, KK, and MK supervised the project; MHL and KK conceptualized the idea; CYK and SAJ synthesized and characterized the pheomelanin-like films with assistance from JSP and JC; JRJ performed and analyzed the electrochemical measurements; MK performed and analyzed the DFT calculations; All authors contributed to the original draft, and MHL, KK, and MK revised the manuscript.

Conflicts of interest

The authors declare that there are no conflicts of interest.

Data availability

The authors confirm that all data supporting the findings of this study are included within the article and its supplementary information (SI). Supplementary information: comprehensive experimental and theoretical data to support the development of metal-free electrocatalytic enhancers based on thin, ultra-smooth pheomelanin-like films derived from DA and cysteine ester derivatives. See DOI: https://doi.org/10.1039/d6sc00776g.

Acknowledgements

This work was supported by the Technology Innovation Program (RS-2024-00419769 to KK and MHL) funded by the Ministry of Trade, Industry & Energy (MOTIE) and by the Basic Research Program (NRF-2021R1A2C2010244 to MHL, RS-2025-16071328 to KK, and RS-2024-00342233 to MK) through the National Research Foundation of Korea (NRF) funded by the Ministry of Science and ICT (MSIT) of the Republic of Korea.

References

1 L. Panzella, G. Gentile, G. D'Errico, N. F. Della Vecchia, M. E. Errico, A. Napolitano, C. Carfagna and M. d'Ischia, *Angew. Chem., Int. Ed.*, 2013, **52**, 12684–12687.
2 D. N. Peles, E. Lin, K. Wakamatsu, S. Ito and J. D. Simon, *J. Phys. Chem. Lett.*, 2010, **1**, 2391–2395.
3 A. Corani, A. Huijser, T. Gustavsson, D. Markovitsi, P.-Å. Malmqvist, A. Pezzella, M. d'Ischia and V. Sundström, *J. Am. Chem. Soc.*, 2014, **136**, 11626–11635.
4 A. B. Mostert, S. B. Rienecker, C. Noble, G. R. Hanson and P. Meredith, *Sci. Adv.*, 2018, **4**, eaaq1293.
5 M. d'Ischia, A. Napolitano, A. Pezzella, P. Meredith and M. Buehler, *Angew. Chem., Int. Ed.*, 2020, **59**, 11196–11205.
6 A. Pira, A. Amatucci, C. Melis, A. Pezzella, P. Manini, M. d'Ischia and G. Mula, *Sci. Rep.*, 2022, **12**, 11436.
7 M. Raffaella, P. Lucia, I. Mariagrazia, O. Crescenzi, K. Kenzo, M. Giuseppe, N. Alessandra and M. D'Ischia, *Pigm. Cell Melanoma Res.*, 2016, **29**, e68.
8 W. Cao, X. Zhou, N. C. McCallum, Z. Hu, Q. Z. Ni, U. Kapoor, C. M. Heil, K. S. Cay, T. Zand, A. J. Mantanona, A. Jayaraman, A. Dhinojwala, D. D. Deheyn, M. D. Shawkey, M. D. Burkart, J. D. Rinehart and N. C. Gianneschi, *J. Am. Chem. Soc.*, 2021, **143**, 2622–2637.
9 A. Napolitano, M. De Lucia, L. Panzella and M. d'Ischia, *Photochem. Photobiol.*, 2008, **84**, 593–599.
10 L. Panzella, L. Leone, G. Greco, G. Vitiello, G. D'Errico, A. Napolitano and M. d'Ischia, *Pigm. Cell Melanoma Res.*, 2014, **27**, 244–252.
11 S. Ito, K. Wakamatsu and T. Sarna, *Photochem. Photobiol.*, 2018, **94**, 409–420.
12 Y. Wang, J. Su, T. Li, P. Ma, H. Bai, Y. Xie, M. Chen and W. Dong, *ACS Appl. Mater. Interfaces*, 2017, **9**, 36281–36289.
13 C. Wang, D. Wang, T. Dai, P. Xu, P. Wu, Y. Zou, P. Yang, J. Hu, Y. Li and Y. Cheng, *Adv. Funct. Mater.*, 2018, **28**, 1802127.

14 J. Lu, J. Fang, J. Li and L. Zhu, *Appl. Surf. Sci.*, 2021, **550**, 149284.
15 B. Poinard, S. Z. Y. Neo, E. L. L. Yeo, H. P. S. Heng, K. G. Neoh and J. C. Y. Kah, *ACS Appl. Mater. Interfaces*, 2018, **10**, 21125–21136.
16 P. Zhang, X. Li, Q. Xu, Y. Wang and J. Ji, *Colloids Surf., B*, 2021, **208**, 112125.
17 X. Zeng, M. Luo, G. Liu, X. Wang, W. Tao, Y. Lin, X. Ji, L. Nie and L. Mei, *Adv. Sci.*, 2018, **5**, 1800510.
18 Y. Kim, E. Coy, H. Kim, R. Mrówczyński, P. Torruella, D.-W. Jeong, K. S. Choi, J. H. Jang, M. Y. Song and D.-J. Jang, *Appl. Catal., B*, 2021, **280**, 119423.
19 D. Aguilar-Ferrer, T. Vasileiadis, I. Iatsunskyi, M. Ziółek, K. Żebrowska, O. Ivashchenko, P. Błaszkiewicz, B. Grześkowiak, R. Pazos, S. Moya, M. Bechelany and E. Coy, *Adv. Funct. Mater.*, 2023, **33**, 2304208.
20 Y.-S. Lim, J. S. Kim, J. H. Choi, J. M. Kim and T. S. Shim, *Colloid Interface Sci. Commun.*, 2022, **48**, 100624.
21 M. Xiao, Y. Li, M. C. Allen, D. D. Deheyn, X. Yue, J. Zhao, N. C. Gianneschi, M. D. Shawkey and A. Dhinojwala, *ACS Nano*, 2015, **9**, 5454–5460.
22 S. Ito and K. Wakamatsu, *Pigm. Cell Res.*, 2003, **16**, 523–531.
23 A. Napolitano, L. Panzella, G. Monfrecola and M. d'Ischia, *Pigm. Cell Melanoma Res.*, 2014, **27**, 721–733.
24 R. B. Deibel and M. R. Chedekel, *J. Am. Chem. Soc.*, 1982, **104**, 7306–7309.
25 Z. Zhang, Z. Yi, J. Wang, X. Tian, P. Xu, G. Shi and S. Wang, *J. Mater. Chem. A*, 2017, **5**, 17064.
26 Y. Lin, K. Shi, Y. Yang, Z. Yang and W. Zhang, *Chem. Eng. Sci.*, 2023, **281**, 119125.
27 D.-D. Wang, X. Gao, L. Zhao, J. Zhou, S. Zhuo, Z. Yan and W. Xing, *RSC Adv.*, 2018, **8**, 16044.
28 K. Qu, Y. Zheng, X. Zhang, K. Davey, S. Dai and S. Z. Qiao, *ACS Nano*, 2017, **11**, 7293–7300.
29 S. Yang, X. Liu, S. Li, W. Yuan, L. Yang, T. Wang, H. Zheng, R. Cao and W. Zhang, *Chem. Soc. Rev.*, 2024, **53**, 5593–5625.
30 Y. Zheng, Y. Jiao, Y. Zhu, L. H. Li, Y. Han, Y. Chen, A. Du, M. Jaroniec and S. Z. Qiao, *Nat. Commun.*, 2014, **5**, 3783.
31 S. Hong, Y. Wang, S. Y. Park and H. Lee, *Sci. Adv.*, 2018, **4**, eaat7457.
32 C. T. Chen, C. Chuang, J. Cao, V. Ball, D. Ruch and M. J. Buehler, *Nat. Commun.*, 2014, **5**, 3859.
33 C. Y. Kim, Y. Kim, M. Y. Lee, S. A. Jo, S.-W. Kim, S. M. Kang, Y.-K. Kim and K. Kang, *Colloids Surf., B*, 2023, **222**, 113068.
34 S. Ryu, J. B. Chou, K. Lee, D. Lee, S. H. Hong, R. Zhao, H. Lee and S. G. Kim, *Adv. Mater.*, 2015, **27**, 3250–3255.
35 H. A. Lee, Y. Ma, F. Zhou, S. Hong and H. Lee, *Acc. Chem. Res.*, 2019, **52**, 704–713.
36 H. Lee, S. M. Dellatore, W. M. Miller and P. B. Messersmith, *Science*, 2007, **318**, 426–430.
37 Y. Liu, K. Ai and L. Lu, *Chem. Rev.*, 2014, **114**, 5057–5115.
38 N. F. Della Vecchia, R. Marega, M. Ambrico, M. Iacomino, R. Micillo, A. Napolitano, D. Bonifazi and M. d'Ischia, *J. Mater. Chem. C*, 2015, **3**, 6525.
39 D. Bogdan, I.-G. Grosu and C. Filip, *Appl. Surf. Sci.*, 2022, **597**, 153680.
40 Y. Ding, L.-T. Weng, M. Yang, Z. Yang, X. Lu, N. Huang and Y. Leng, *Langmuir*, 2014, **30**, 12258–12269.
41 J. Yu, T. M. D'Alvise, I. Harley, A. Krysztofik, I. Lieberwirth, P. Pula, P. W. Majewski, B. Graczykowski, J. Hunger, K. Landfester, S. L. Kuan, R. Shi, C. V. Synatschke and T. Weil, *Adv. Mater.*, 2024, **36**, 2401137.
42 R. Qie, S. Z. Moghaddam and E. Thormann, *Phys. Chem. Chem. Phys.*, 2021, **23**, 5516–5526.
43 Z.-H. Huang, S.-W. Peng, S.-L. Hsieh, R. Kirankumar, P.-F. Huang, T.-M. Chang, A. K. Dwivedi, N.-F. Chen, H.-M. Wu and S. Hsieh, *Materials*, 2021, **14**, 671.
44 R. A. Zangmeister, T. A. Morris and M. J. Tarlov, *Langmuir*, 2013, **29**, 8619–8628.
45 M. Li, L. Zhang, Q. Xu, J. Niu and Z. Xia, *J. Catal.*, 2014, **314**, 66–72.
46 S. Zhou, N. Liu, Z. Wang and J. Zhao, *ACS Appl. Mater. Interfaces*, 2017, **9**, 22578–22587.
47 J. Jung, H. Lim, J. Oh and Y. Kim, *J. Am. Chem. Soc.*, 2014, **136**, 8528–8531.
48 M. Kang, E. Kim, Z. Temoçin, J. Li, E. Dadachova, Z. Wang, L. Panzella, A. Napolitano, W. E. Bentley and G. F. Payne, *Chem. Mater.*, 2018, **30**, 5814–5826.
49 W. Cao, N. C. McCallum, Q. Z. Ni, W. Li, H. Boyce, H. Mao, X. Zhou, H. Sun, M. P. Thompson, C. Battistella, M. R. Wasielewski, A. Dhinojwala, M. D. Shawkey, M. D. Burkart, Z. Wang and N. C. Gianneschi, *J. Am. Chem. Soc.*, 2020, **142**, 12802–12810.
50 W. Cao, H. Mao, N. C. McCallum, X. Zhou, H. Sun, C. Sharpe, J. Korpanty, Z. Hu, Q. Z. Ni, M. D. Burkart, M. D. Shawkey, M. R. Wasielewski and N. C. Gianneschi, *Chem. Sci.*, 2023, **14**, 4183–4192.
51 M. J. Frisch, G. W. Trucks, H. B. Schlegel, G. E. Scuseria, M. A. Robb, J. R. Cheeseman, G. Scalmani, V. Barone, G. A. Petersson, H. Nakatsuji, X. Li, M. Caricato, A. V. Marenich, J. Bloino, B. G. Janesko, R. Gomperts, B. Mennucci, H. P. Hratchian, J. V. Ortiz, A. F. Izmaylov, J. L. Sonnenberg, D. Williams-Young, F. Ding, F. Lipparini, F. Egidi, J. Goings, B. Peng, A. Petrone, T. Henderson, D. Ranasinghe, V. G. Zakrzewski, J. Gao, N. Rega, G. Zheng, W. Liang, M. Hada, M. Ehara, K. Toyota, R. Fukuda, J. Hasegawa, M. Ishida, T. Nakajima, Y. Honda, O. Kitao, H. Nakai, T. Vreven, K. Throssell, J. A. Montgomery Jr, J. E. Peralta, F. Ogliaro, M. J. Bearpark, J. J. Heyd, E. N. Brothers, K. N. Kudin, V. N. Staroverov, T. A. Keith, R. Kobayashi, J. Normand, K. Raghavachari, A. P. Rendell, J. C. Burant, S. S. Iyengar, J. Tomasi, M. Cossi, J. M. Millam, M. Klene, C. Adamo, R. Cammi, J. W. Ochterski, R. L. Martin, K. Morokuma, O. Farkas, J. B. Foresman and D. J. Fox, *Gaussian 16, Revision C.01*, Gaussian, Inc., Wallingford CT, 2016.
52 P. J. Stephens, F. J. Devlin, C. F. Chabalowski and M. J. Frisch, *J. Phys. Chem.*, 1994, **98**, 11623–11627.
53 K. Momma and F. Izumi, *J. Appl. Crystallogr.*, 2011, **44**, 1272–1276.
54 J. Tomasi, B. Mennucci and R. Cammi, *Chem. Rev.*, 2005, **105**, 2999–3094.

55 A. A. Peterson, F. Abild-Pedersen, F. Studt, J. Rossmeisl and J. K. Nørskov, *Energy Environ. Sci.*, 2010, **3**, 1311–1315.
56 G. Kresse and J. Furthmüller, *Phys. Rev. B*, 1996, **54**, 11169.
57 J. P. Perdew, K. Burke and M. Ernzerhof, *Phys. Rev. Lett.*, 1996, **77**, 3865.
58 S. Grimme, S. Ehrlich and L. Goerigk, *J. Comput. Chem.*, 2011, **32**, 1456–1465.
59 G. Kresse and D. Joubert, *Phys. Rev. B*, 1999, **59**, 1758.
60 H. J. Monkhorst and J. D. Pack, *Phys. Rev. B*, 1976, **13**, 5188.
61 W. Tang, E. Sanville and G. Henkelman, *J. Phys.: Condens. Matter*, 2009, **21**, 084204.